

Temperature Slope Crystallization of Polymers (A survey of polymer crystallization by X-ray diffraction . chapter 5)

メタデータ	言語: en 出版者: SKP 公開日: 2008-01-31 キーワード (Ja): キーワード (En): 作成者: Asano, Tsutomu, Mina, Md. Forhad メールアドレス: 所属:
URL	<a href="http://hdl.handle.net/10297/552">http://hdl.handle.net/10297/552</a>

## 5.4 TSC of paraffin and polyethylene

### 5.4.1 Observation of the melt-solid boundary

Linear hydrocarbon molecules, called n-alkane, have a chemical conformation of  $C_nH_{2n+2}$ . Normally, we call paraffin when  $10 < n < 50$ . In order to observe the crystallizing boundary, we used several paraffins which we abbreviated by the notation of the carbon numbers :C(n). The longer hydrocarbon molecule with average molecular weight being 2000 (corresponding to the carbon number:  $n = 142-143$ ) is called polyethylene 2000 (PE2000). To observe the melt-solid boundary, the sample was put in a glass capillary and set to the TSC apparatus. The heater was controlled at a definite temperature above the melting point of the sample, which was fixed at 170 °C for PE2000 and at 110 °C for C32, C36, and C38. The temperature of the cooler was 25 °C by continuous circulation of water. Then, the temperature slope was set up in a gap of 2 mm between the heater and the cooler [15].

The average temperature slope at the center of the gap was measured as 30°C/mm for PE2000 and 15°C/mm for paraffins. The glass capillary was then moved downwards with a velocity,  $V = 1.0$  mm/hr. The features of the crystal growth plane were monitored by a polarized optical microscope with suitable magnification. The results were displayed by a television using a CCD camera, and the data were recorded on a video tape. We define the z-axis along the temperature slope, parallel to the sample capillary.

Figure 5.7 provides a microscopic view of the melt-solid boundary for PE2000. In Fig.5.7a, a stationary melt-solid boundary appears at the position shown by an arrow. When the sample is stopped in between the heater and the cooler, the temperature of the boundary is considered to coincide with the melting point ( $T_m = 132.6$  °C) of PE2000. In Fig.5.7b, the sample capillary is moved downwards by 1 mm/hr along the z-axis. *Under the crystallization condition, the melt-solid boundary is shifted downward. A new region between the two surfaces of Figs. 5.7(a) and 5.7(b) corresponds to a supercooled state with the melt temperature lower than  $T_m$ .*

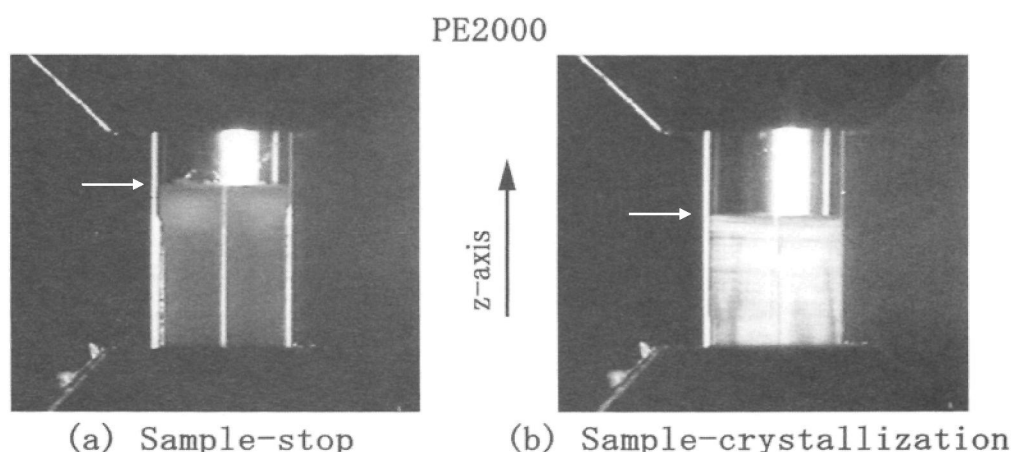


Fig. 5.7 a) Sample-stop and b) sample-crystallization stage, representing the difference in height of the melt-solid boundaries as indicated by arrows [15].

In the case of the even-number paraffins, such as C32 and C36, the melt-solid boundary did not show any shifting downward by TSC. *Contrary to the cases of PE2000 and other polymer samples, the crystal growth planes of some even-number paraffins are shifted to the higher temperature.* The shift increased with the crystallizing time and stopped when the surface moved about 0.3 mm up from the original position in the case of C36. Considering the temperature slope, the shift corresponds to 4.5 °C upper than the melting temperature.

In our additional measurements using the odd-number paraffins such as C29 and C33, the crystal growth plane did not show any shifting upward, but rather was shifted slightly downward. The resultant orientation observed by the X-ray diffraction was very broad, without sharp lamellar orientation as observed for the even-number paraffins.

#### 5.4.2 *In-situ* X-ray measurement of PE2000

The *in-situ* X-ray measurements were performed at the synchrotron facility using a high brightness incident beam with 7 $\mu$ m in diameter. WAXS and SAXS patterns of PE2000 crystallized by TSC are shown in Fig. 5.8. From the position of 110 and 200 reflections in Fig.5.8a, the crystal has a b-axis orientation parallel to the z-axis. The SAXS pattern shows that lamellae are well developed by TSC, where the normal are oriented perpendicular to the z-axis.

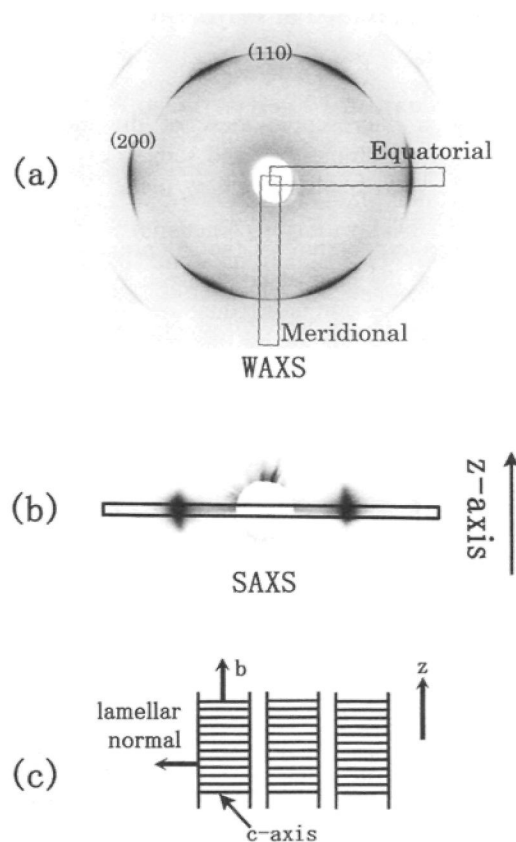


Fig. 5.8 (a) WAXS and (b) SAXS patterns of PE2000 at the TSC growth surface.  
(c) Schematic illustration of the lamellar and c-axis orientation at the growth front. [15]

In order to measure the intensity profile along the equator (E) and meridian (M), integrated intensities of the rectangular areas in Fig.5.8a were compared. For the SAXS pattern, the equatorial intensity was integrated in the rectangular region in Fig.5.8b. The features of lamellar and molecular orientation are illustrated in Fig.5.8c. The spacing of the lamellae is measured 180 Å. As this value coincides to the molecular length of PE2000, the molecule is extended in the lamella.

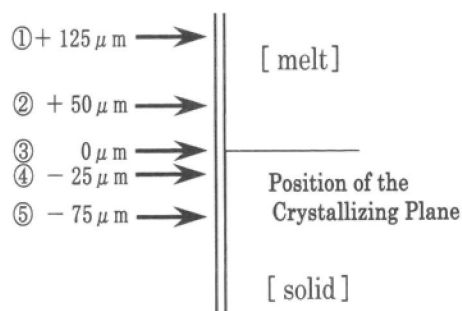


Fig. 5.9 Positions of the incident X-ray beam; the crystallizing surface is adjusted to 0  $\mu\text{m}$ . [15]

The positions of the incident beam are shown in Fig. 5.9. Positions ① and ② are in the supercooled state above the crystallizing surface. Position ③ is adjusted on the crystallizing surface, and positions ④ and ⑤ are under the surface.

The results of the *in-situ* measurements are summarized in Fig. 5.10. The WAXS profiles obtained for supercooled melt at +125 and +50  $\mu\text{m}$  show absolutely no difference between E and M intensity. This means that molecules in this state are completely at random orientation. The diffuse peak indicates an amorphous state without crystalline order. When the incident X-ray is adjusted at the crystallizing surface (0  $\mu\text{m}$ ), the amorphous intensities of E and M again do not show any conspicuous difference. A sharp crystalline peak is found at an angle about  $2\theta=24^\circ$  on the equatorial profile (E), indicating 200 reflection. In WAXS at positions ④ and ⑤, the crystalline peaks become stronger with sharp orientation. The corresponding profiles have peaks of the 110 reflection on M and a strong 200 reflection on E.

At the position -25  $\mu\text{m}$  below the surface, the amorphous intensity of the WAXS patterns decreases, and a slight difference of intensity between the two profiles appears; the (M) profile is higher than (E). At -75  $\mu\text{m}$ , the meridional intensity of the amorphous curve is obviously stronger than the equatorial one, suggesting that the amorphous molecules are slightly oriented perpendicular to the z-axis.

The intensity profiles for the SAXS patterns are also compared in Fig. 5.10. To discuss the amount of long range order, the SAXS intensity  $I$  (arbitrary unit) was multiplied by the reciprocal unit  $s$  ( $= 1/d$ ). This correction is performed based on the assumption of uniaxial symmetry of the structure near the crystallizing plane.

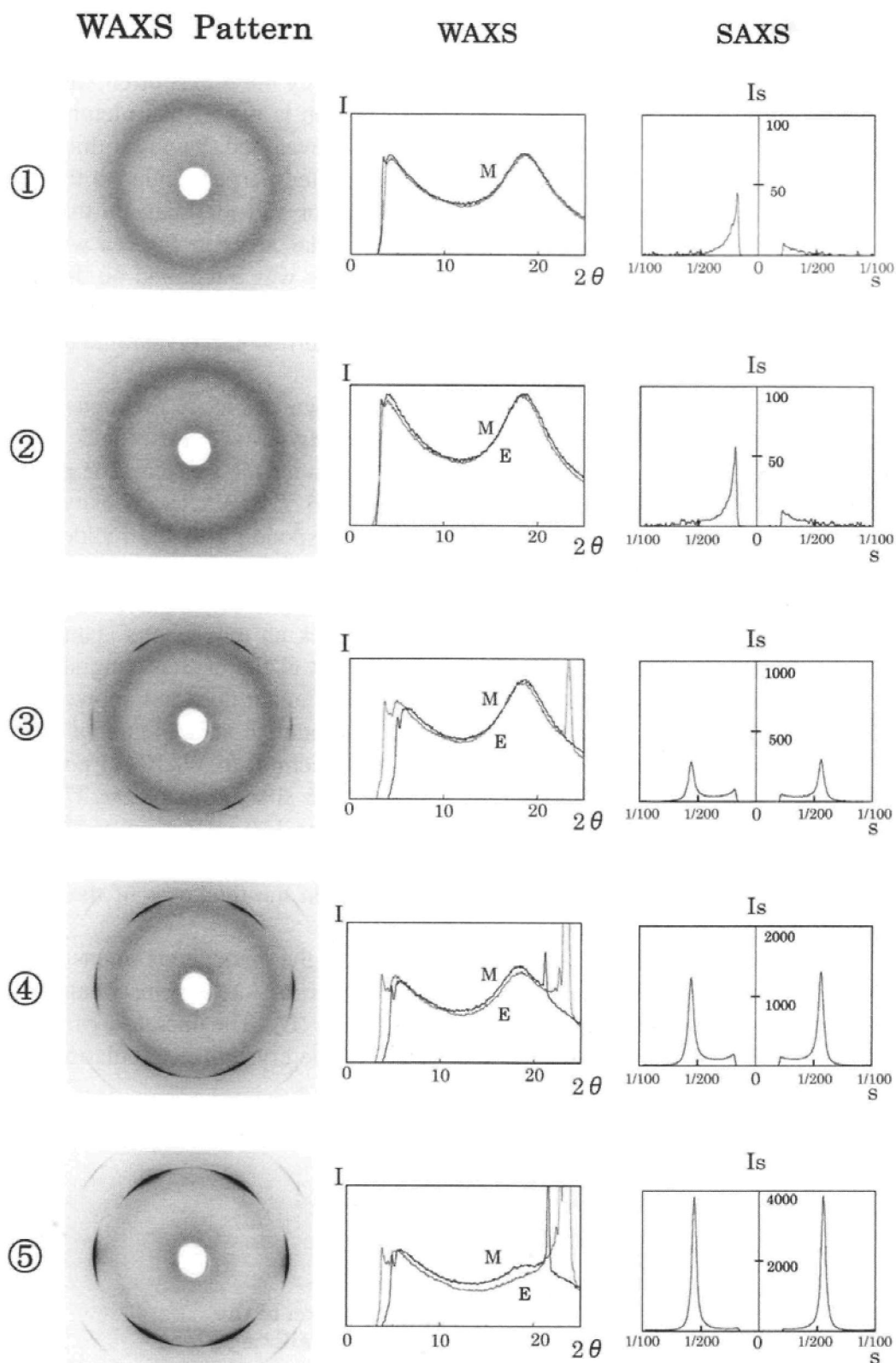


Fig. 5.10 Summary of the *in-situ* measurements of PE2000. For WAXS patterns, equatorial (E) and meridional (M) intensities (I, arbitrary unit) are plotted as the diffraction angle ( $2\theta$ ). The corrected SAXS intensity ( $I \times s$ ) is plotted as the reciprocal unit  $s$  ( $=1/d$ ) [15].

The SAXS peaks are observed at  $s = 0.0055 \text{ \AA}^{-1}$  ( $180 \text{ \AA}$ ) when the X-ray beam is under the crystallizing plane (positions ③, ④, and ⑤). In case of  $+125 \mu\text{m}$ , the SAXS intensity increases at an  $s$  value lower than  $0.0055 \text{ \AA}^{-1}$ , indicating that a density fluctuation larger than  $180 \text{ \AA}$  is present in the supercooled region. At the position of  $+50 \mu\text{m}$  (position ②), the  $I_s$  value is higher than that of the position ①. The result indicates that *the precursor long range order is appeared in the melt state near the crystallizing plane.*

#### 5.4.3 In-situ TSC of C36

*In situ* X-ray measurements on paraffin (C36) were performed by TSC. As shown in Fig.5.11, the incident X-ray is fixed at  $0 \mu\text{m}$ . When the sample capillary is moved downward, the crystallizing surface moves upward. The WAXS patterns are compared when the interface is at  $0 \mu\text{m}$  (sample-stop) and  $+40 \mu\text{m}$  (sample crystallizing). At the crystallizing front, sharply oriented lamellar reflections appear on the meridian, showing that the normal of the lamellae is parallel to the  $z$ -axis. The equatorial WAXS reflections indicate that the pseudohexagonal packing of the rotator phase has some molecular inclination from the  $z$ -axis. The structure model of even-number paraffins is shown in Fig.5.11c. The crystalline orientation of C36 is totally different from that of PE2000 shown in Fig.5.8c.

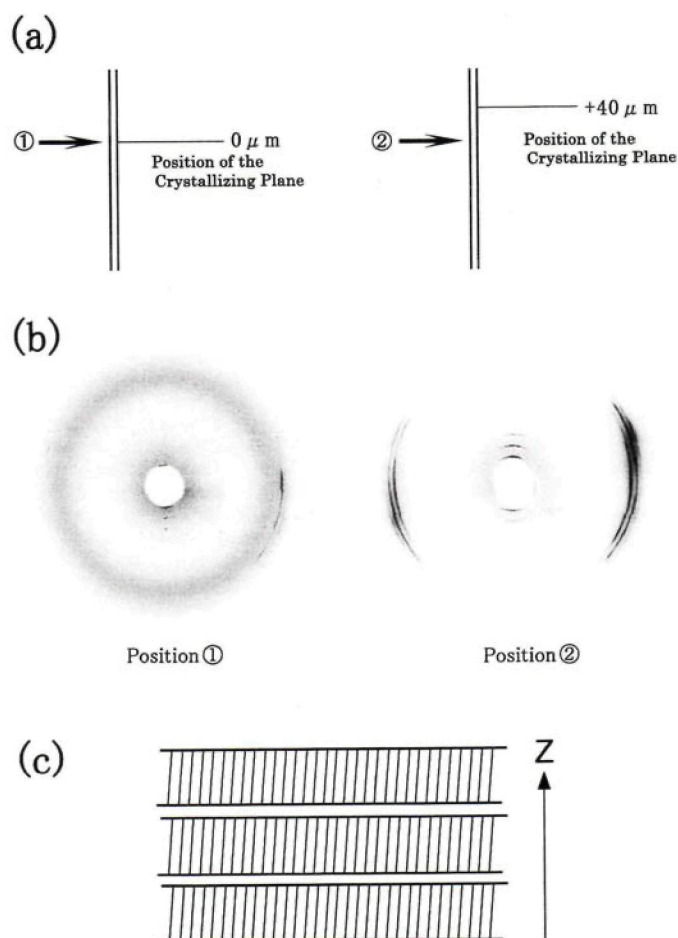


Fig. 5.11 *In-situ* WAXS measurements of C36. The meridional reflections indicate that lamellae are oriented such that their normal is parallel to the  $z$ -axis [15].

#### 5.4.4. Dynamic features of TSC

##### 5.4.4.1 Lamellar and molecular orientation

We have performed extensive studies of TSC on paraffins and polyethylenes. The results are classified into three categories [16]:

1. *Both lamellar normal and crystalline c-axis are perpendicular, where the b-axis is parallel to the z-axis. This type of orientation appears in PE2000 and longer chain PE.*
2. *Both lamellar normal and crystalline c-axis are nearly parallel to the z-axis, as shown in the even number paraffins such as C36, C32 and C28.*
3. Both lamellar and crystalline reflections are broadly distributed without showing sharp orientation. This type appeared in C20-C27, C29, C30-C33.

##### 5.4.4.2 Movement of the crystallizing plane

In the TSC method, the crystallizing surface is normally shifted downwards as appeared in PE2000. This movement is consistent if we consider a supercooled region before crystallization. However, the even-number paraffin shows a special movement of the crystallizing surface moving to higher temperatures. This fact cannot be explained if we consider that the original position of the sample-stop surface is adjusted to the melting point ( $T_m$ ) of the paraffins, because the upper crystallization then occurs at a higher temperature than  $T_m$ .

Normally, long chain molecules can easily assemble with each other producing a lamellar structure. Then, both molecular c-axis and lamellar normal become perpendicular to the z-axis, as shown in PE2000. However, if we imagine crystal growth by a screw dislocation, a perpendicular orientation can be explained, with a lamellar normal parallel to the z-axis. The crystallizing surface of the even-number paraffins is moved to a higher position by reinforcement of the crystallites by the preferred nucleation and orientation associated by the screw dislocation.

##### 5.4.4.3 Structure in the supercooled region

In the WAXS profiles of Fig. 5.10, the amorphous intensity show anisotropy at  $-25$  and  $-75$   $\mu\text{m}$ ; the meridional reflection being stronger than equatorial one. This fact indicates that the amorphous molecules are slightly oriented perpendicular to the z-axis. However, for amorphous molecules in the supercooled state ( $+125$  and  $+50$   $\mu\text{m}$ ) and even at the crystallizing surface ( $0$   $\mu\text{m}$ ), there is no apparent molecular orientation.

More information of the supercooled melt state has been observed in the SAXS pattern, indicating long-range density fluctuation. The long range density fluctuations in polymer melts have been discussed by several authors [24, 25]. In this experiment with PE2000, the SAXS intensity in Fig.5.10 at the positions  $+125$  and  $+50$   $\mu\text{m}$  has a weak peak at the position around  $s=0.005$   $\text{\AA}^{-1}$ . The result suggests that the supercooled melt has a long-range fluctuation slightly larger ( $\sim 200$   $\text{\AA}$ ) than the final  $180$   $\text{\AA}$  lamellar periodicity.

## 5.5 TSC of isotactic polypropylene (iPP)

### 5.5.1 Crystalline phases of iPP

Isotactic polypropylene (iPP) is known to have several crystalline phases, labeled  $\alpha$ ,  $\beta$ , and  $\gamma$  [26, 27]. The major form of iPP is known to have the  $\alpha$  and  $\beta$  phases at atmospheric pressure with monoclinic and hexagonal structure, respectively. The crystalline orientation of iPP by TSC was reported by Fujiwara and Asano [6, 11].

Figures 5.5 and 5.6 indicate the micrographs and X-ray diffraction patterns of the two different phases of PP, respectively. Because of excess  $\alpha$ -nucleation frequency, the initial sample was occupied by the oriented  $\alpha$ -phase. As a result of the faster growth rate, the  $\beta$ -phase texture developed preferentially from a  $\beta$ -nucleus and soon occupied the entire available space of the sample. Thus, the appearance of a  $\beta$ -nucleus changed the structure completely from the  $\alpha$ -phase to the  $\beta$ -phase as shown in Fig.5.5b. The crystalline orientation of the  $\alpha$ - and  $\beta$ -phase crystals was determined by WAXS measurement, as shown in Fig. 5.6. The  $\alpha$ - and  $\beta$ -crystals have a uniaxial orientation with the  $a^*$ - and  $a$ -axis being parallel to the  $z$ -axis, respectively.

### 5.5.2 Methodology of TSC for iPP

For TSC of iPP, the heater temperature was fixed to 220 °C and the cooler was kept at 20 °C. The glass capillary containing iPP was moved downward with a velocity,  $V = 1.15$  mm/hr (0.32  $\mu\text{m}/\text{sec}$ ). We used two sets of apparatus: one was for the optical measurement and the other was for the *in-situ* X-ray measurement. The gap distance (2 mm) and the temperatures of the heater and the cooler, and the velocity of the sample capillary were same in both apparatuses. Cylindrical and conical shaped heater and cooler were used for the both equipments.

The temperature slope of the optical TSC was checked by a micro-thermocouple with very thin copper and constantan wires. The micro-thermocouple was put into the glass capillary, where the copper and constantan wires were bound to opposite sides of the capillary. The iPP rod was re-melted to fill in the capillary. It was difficult to measure the exact temperature slope, because the gradient was not linear in the gap. The sample temperature at the upper side was lower than that of the heater, and that at the bottom side was higher than the cooler temperature. The diameter of the glass capillary also affected the temperature gradient. As a result, the average value of the temperature slope was measured as 50 °C/mm.

We define here the  $z$ -axis parallel to the temperature slope. In a sample-stop (SS) stage, before the TSC runs, the melt-solid boundary appeared at a fixed position below the heater. The movement of the boundary was measured by an optical microscope monitored by a video system. During the steady-state TSC, the crystalline growth rate  $G$  coincided with moving speed  $V$ . The resulting crystal exhibited one directional orientation along the  $z$ -axis.

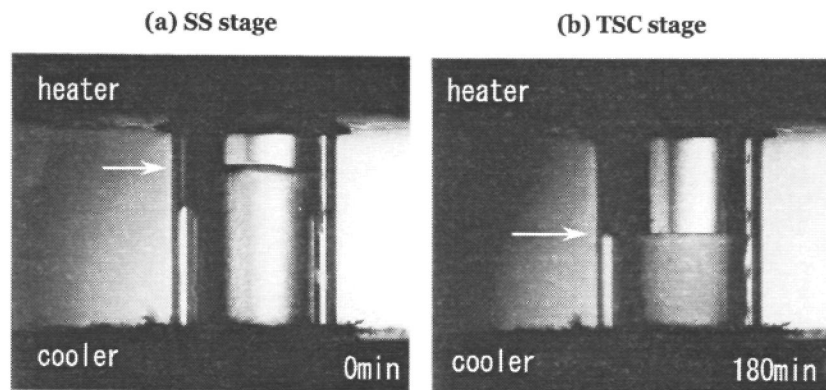


Fig. 5.12 (a) SS (Sample Stop) stage and (b) TSC stage representing the difference in height of the melt-solid boundary as indicated by arrows [20].

### 5.5.3 Optical measurements on the melt-solid boundary

When the sample capillary was stopped (SS stage), the melt-solid boundary appeared 1600  $\mu\text{m}$  above the cooler [Fig. 5.12a]. This position on the sample capillary is named as  $Z_0$ . Then TSC was started by moving the sample capillary downward with the speed  $V$ . The boundary was moved downward until stationary TSC was maintained. Figure 5.12b shows the position of the melt-solid surface after 180 min. The difference of the two interfaces (arrows in Fig. 5.12) indicates the supercooled region corresponding to 700  $\mu\text{m}$ . Since the average temperature gradient is of 50  $^{\circ}\text{C}/\text{mm}$ , amount of the supercooling corresponds to  $-35^{\circ}\text{C}$ . In the TSC, iPP was stationary crystallized at the boundary with the growth rate  $G=1.15$  mm/hr.

Movement of the boundary with respect to time was measured by the optical microscope. The results, averaged for three measurements, are shown in Fig. 5.13. The movement of the glass capillary (the position of  $Z_0$ ) is indicated by a dotted line.

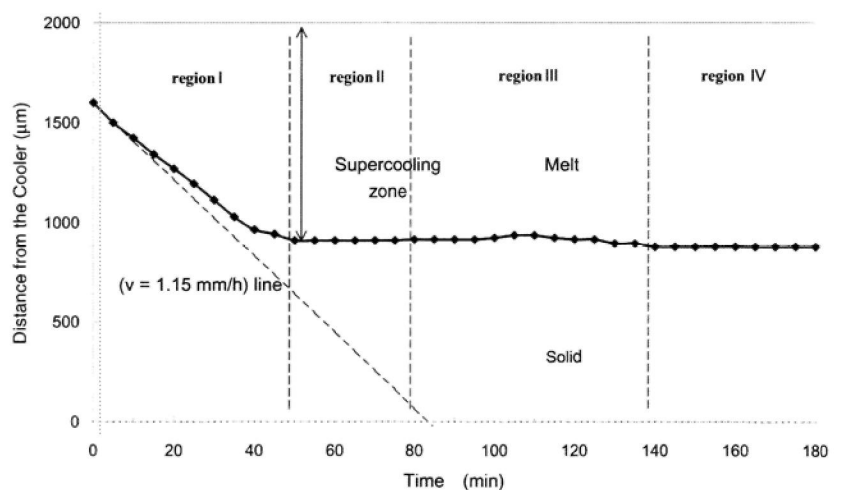


Fig. 5.13 Movement of the melt-solid boundary as a function of the crystallizing time [20].

We define four regions in Fig.5.13. In region I, the boundary moves downward with the glass capillary. Starting the primary crystallization at the end of this region, position of the boundary is removed from  $Z_0$ . At region II, TSC develops by the large supercooling;  $35^\circ\text{C}$  lower than the melting temperature. As oriented  $\alpha$ -phase is developed by  $V$ , the surface is fixed to the same position. After appearance of a  $\beta$ -nucleus, the  $\alpha$ -crystals decrease while  $\beta$ -crystals increase in region III. The oriented  $\beta$ -phase occupies the whole capillary in region IV. The time scales of the regions II-IV are shortened by an appearance of  $\beta$ -nucleation. In some cases of rapid  $\beta$ -nucleation, the  $\beta$ -phase crystal appears before 60 min.

#### 5.5.4 X-ray diffraction measurements

*In-situ* WAXS and SAXS measurements using synchrotron radiation with a  $7\ \mu\text{m}$  pinhole collimation were performed by means of imaging plate. The position of WAXS IP was displaced from the direct beam so as not to disturb the pattern of SAXS. To shift the position of the incident X-ray beam on the sample, the TSC apparatus was moved downward at a constant velocity of  $5\ \mu\text{m}/\text{sec}$  by a stepping motor. Besides, IPs of WAXS and SAXS were simultaneously moved with  $0.4\ \text{mm}/\text{sec}$  parallel to the  $z$ -axis. An equatorial masking slit with a width of  $2\ \text{mm}$  was placed in front of the IP films. The scattered intensity was monitored only on the equator passing the slit. For scanning from bottom to top of the gap ( $2000\ \mu\text{m}$ ) by  $5\ \mu\text{m}/\text{sec}$ , one measurement took 400 sec. Simultaneously, WAXS and SAXS IPs and the sample capillary were moved by  $0.4\ \text{mm}/\text{sec}$  and by  $0.32\ \mu\text{m}/\text{sec}$ , respectively. In addition, position resolved SAXS pattern was measured by a CCD camera connected to a computer system with exposure time of 30 sec for each pattern.

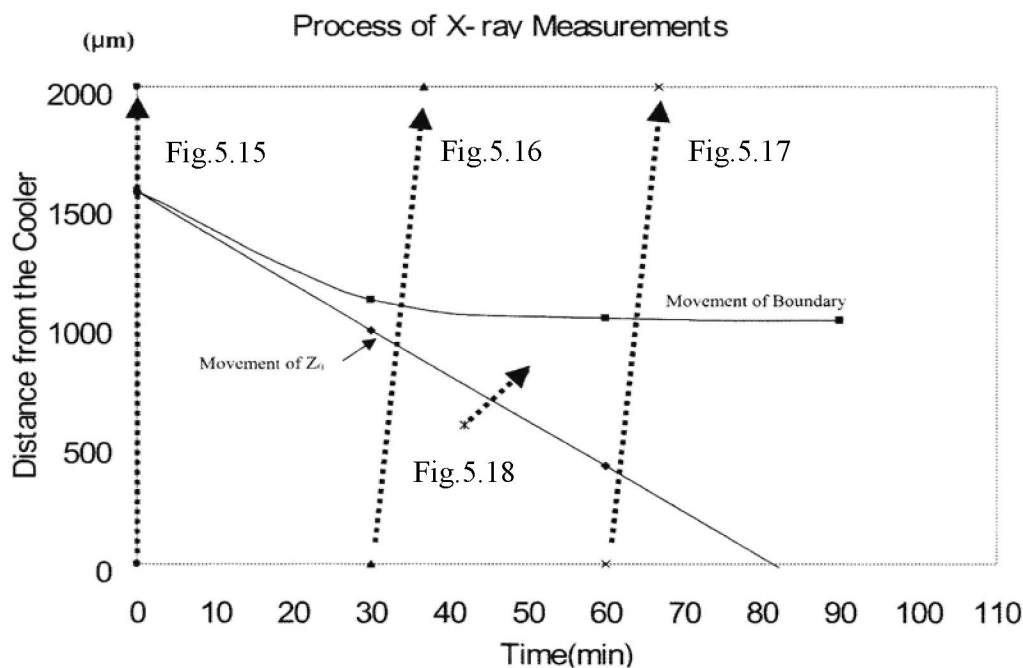


Fig. 5.14 Process of X-ray measurements during the *in-situ* TSC.[20]

### 5.5.5 Process of X-ray measurements

To explain the X-ray measurements, the experimental process is shown in Fig. 5.14. The position of the melt-solid boundary was scaled by the distance from the cooler and analyzed by the X-ray results. The starting time of the X-ray measurements is adjusted to the starting time of the TSC run. We call the time along horizontal axis as crystallizing time. The synchronized measurement was performed at different crystallizing times ( $t$ ) and with different X-ray exposing times ( $t_e$ ). The processes of these measurements are indicated by arrows in Fig. 5.14. The results observed with  $t = 0$  (sample stop) is shown in Fig. 5.15, with  $t = 30$  min &  $t_e = 400$  sec (6.7 min) is in Fig. 5.16, with  $t = 42$  min &  $t_e = 8$  min is in Fig. 5.18, and with  $t = 60$  min &  $t_e = 400$  sec is shown in Fig. 5.17. During these measurements, the position of  $Z_0$  was moved by the velocity of 1.15 mm/hr ( $19\mu\text{m}/\text{min}$ ).

By moving the TSC apparatus, the SAXS and WAXS equatorial reflections were simultaneously and continuously measured on the IP films as shown in Figs. 5.15, 5.16 and 5.17. Because of the rapid  $\beta$ -nucleation during these measurements, the region III appeared before 60 min. The WAXS pattern of Fig. 5.15 indicates that the initial crystalline form of iPP was the  $\alpha$ -phase. The arrows on the SAXS and WAXS patterns show the melt-solid boundary at  $Z_0$ . The SAXS pattern is shifted to a smaller angle when the incident beam approaches the melt-solid boundary. Due to the temperature slope, the crystalline lamellae grow thicker while approaching to  $Z_0$ . The masked SAXS pattern clearly shows the thermal thickening of the  $\alpha$ -phase lamellae. Both the WAXS and SAXS crystalline reflections disappear above the boundary.

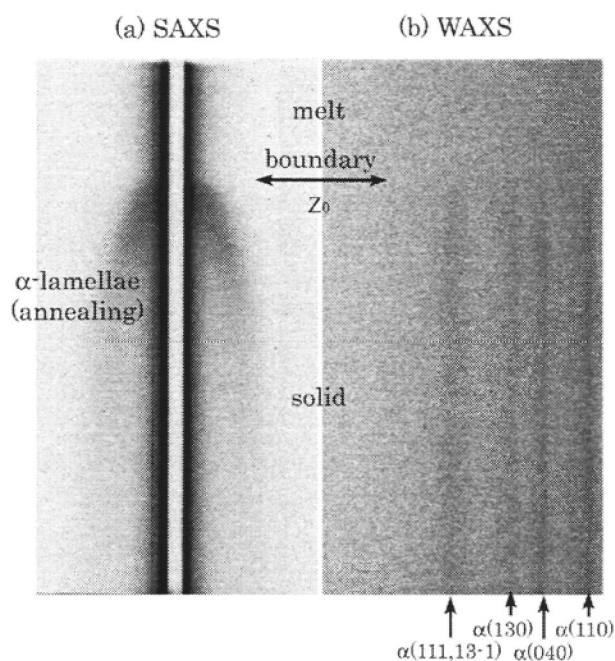


Fig. 5.15 Continuous equatorial pattern,  $t = 0$  (Sample Stop), measured by the masking slit [20].

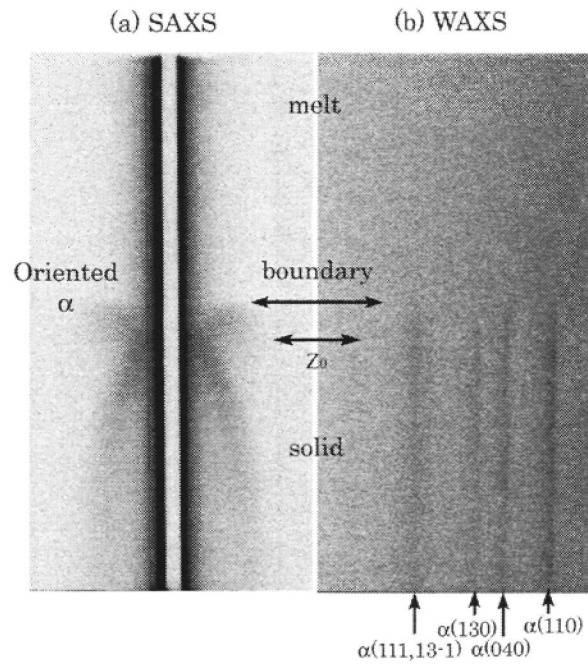


Fig. 5.16 Continuous equatorial pattern,  $t = 30$  min,  $t_e = 400$ s, measured by the masking slit [20].

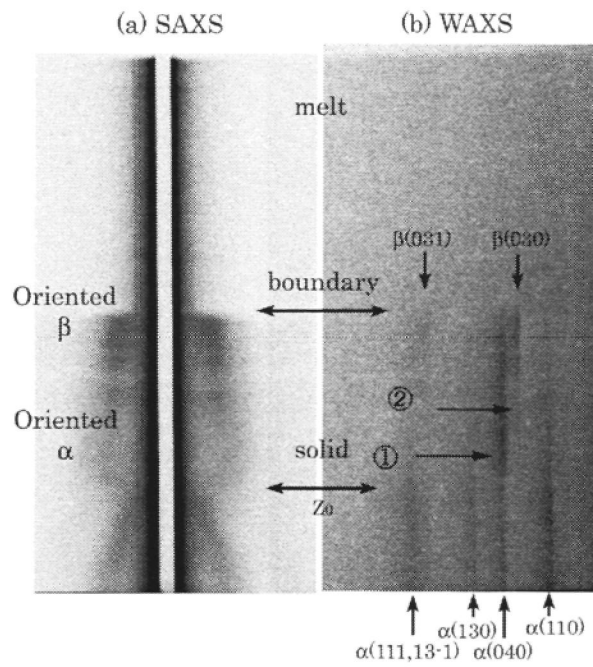


Fig. 5.17 Continuous equatorial pattern,  $t = 60$ min,  $t_e = 400$ sec [20].

The position of the boundary is lowered in Fig. 5.16. After starting the TSC, the SAXS peak rapidly develops at a larger angle. This fact indicates that the lamellae of the TSC are relatively thin due to the increase of supercooling. As the WAXS pattern indicates  $\alpha$ -phase reflections, the initial crystallization is developed by the  $\alpha$ -phase crystals.

At arrow ① of Fig. 5.17, the  $\alpha$ -phase 040 reflection becomes intense showing appearance of the  $a^*$ -orientation of the  $\alpha$ -crystal. The  $\beta$  030 reflection appears at the position of arrow ②. The SAXS pattern shows coexistence of the  $\alpha$ - and  $\beta$ -phase reflections. The original boundary  $Z_0$  at the SS stage is moved downward to 1150  $\mu\text{m}$  by the 60-min TSC run. The whole story of the TSC was memorized on the sample along the  $z$ -axis.

With the help of the pinhole collimation, the crystallizing boundary was observed by position resolved SAXS measurements. Using a very high intensity of the synchrotron radiation beam, SAXS were measured at positions around  $Z_0$  as shown in Fig. 5.14. In Fig. 5.18, the distance  $z$  is fixed by taking into account the movement of  $Z_0$  during the measurement. The negative positions show the annealing phenomena because the sample below  $Z_0$  has not melted during its thermal history. For the positive positions, the molecules are once melted and then recrystallized by the TSC. The intensity profiles of Fig. 5.18 were modified by a computer gradation technique that clearly emphasized the intensity contour.

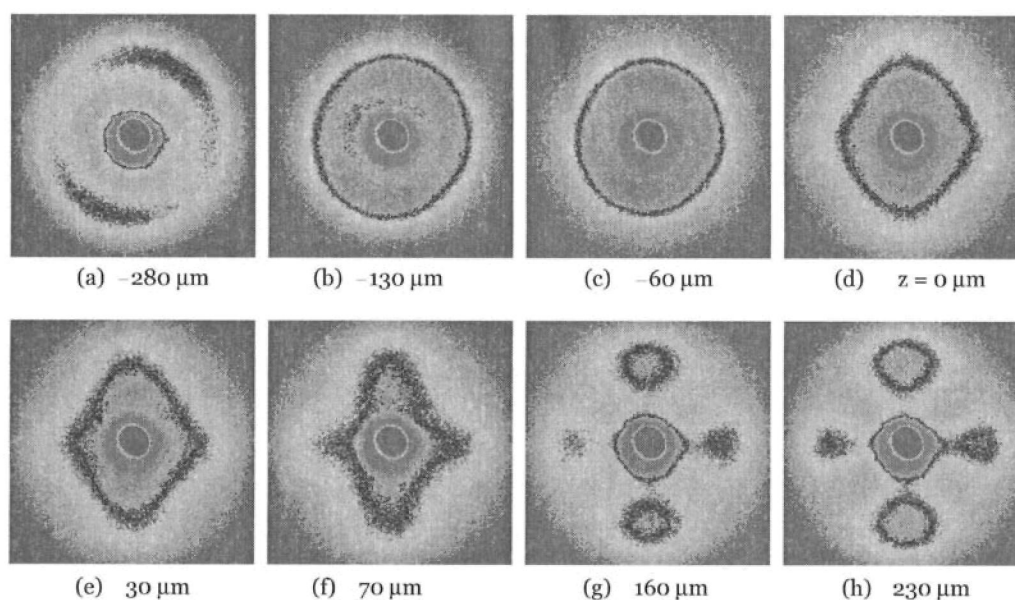


Fig. 5.18 Position-resolved SAXS patterns,  $t = 42\text{min}$ ,  $t_e = 8 \text{ min}$  [20].

The position of the incident beam is scaled from  $Z_0$  on the equator.

Figure 5.18(a)–(c) indicates that the ring patterns are shifted to smaller angles with a slight intensification on the meridian. This fact reveals that slight lamellar orientation occurs, accompanying by the layer thickening process during the annealing. From Fig. 5.18(d)–(f) the SAXS peaks shows strong intensity on the meridian, while it is difficult to distinguish the peak. The results strongly indicate that the initial  $\alpha$ -phase crystallization increases the meridional scattering. Then Fig. 5.18(g) and (h) show the typical cross pattern, where the peaks clearly appear on both the equator and the meridian. This pattern was first observed by Fujiwara for the oriented  $\alpha$ -phase crystallized by the TSC method [6].

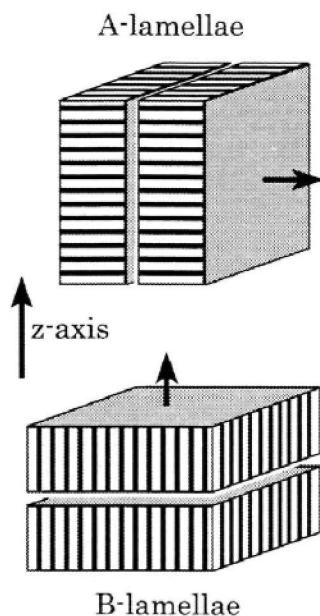


Fig. 5.19 Schematic model of A- and B-lamellae. Equatorial- and meridional peaks in Fig. 5.18 are from A- and B lamellae, respectively [20].

### 5.5.6 Mechanism of iPP crystallization

In Fig. 5.19, we define A- and B-lamellae, where the normal and  $c$ -axis of the former are perpendicular and of the latter are parallel to the  $z$ -axis. In these circumstances, the SAXS reflections of A- and B-lamellae will appear on the equator and on the meridian, respectively. The important experimental results are summarized as follows:

- i. In the sample-stop condition, the  $\alpha$ -phase lamellae become thicker while approaching to the melt-solid boundary due to annealing effects. Close to the melt-solid boundary, the SAXS reflection becomes intensified on the meridian, *indicating that B-lamellae are stable*.
- ii. In the beginning of the TSC experiment, the  $\alpha$ -phase B-lamellae develop as the primary process of crystallization. On the secondary crystallization under high supercooling, the SAXS cross pattern indicates *appearance of the  $\alpha$ -phase A- and B-lamellae*. Due to the supercooling, *thickness of the secondary lamellae is thinner than that of the primary ones*.
- iii. Subsequently, the oriented  $\alpha$ -phase lamellae are replaced by oriented  $\beta$ -phase lamellae. Following the appearance of a spontaneous  $\beta$ -nucleus, *the  $\beta$ -phase lamellae grow preferentially, excluding the  $\alpha$ -phase, and occupy the whole area of the sample*.

During the *in-situ* TSC measurement, the melt-solid boundary appears perpendicular to the z-axis. The original iPP sample in the capillary is as-grown spherulite crystals in which both A- and B-lamellae are equally existed. As the *c*-axes of A-lamellae are parallel to the boundary, molecules are easy to be detached from the crystals at the boundary. On the other hand, molecules of the B-lamellae are difficult to melt, because their *c*-axis is perpendicular to the boundary, and hence they are buried in the lamellae. As a result, the thick B-lamellae are more stable near the melt-solid boundary in the SS stage.

Starting from the TSC run, the initial crystallization develops on the boundary. As it is difficult to form a new nucleus near the melting temperature, the initial crystallization starts from the remaining B-lamellae. Thus the SAXS reflection first becomes intense on the meridian due to the newly crystallized B-lamellae, as indicated in Fig. 5.18(e). As the growth direction of the B-lamellae is perpendicular to the z-axis, the possible growth mechanism is the screw dislocation. However, the growth rate is slow in the primary crystallization.

When the glass capillary is moved to downward, the crystallizing interface moves to a lower temperature. Due to the higher supercooling, the frequency of the  $\alpha$ -phase nucleation increases. In this case, the growth of A-lamellae gets advantage because the growth direction of the A-lamellae is parallel to the z-axis. Accordingly, in the second stage of crystallization, the A-lamellae grow faster at the boundary. Then, the iPP *c*-axis lies epitaxially on the side surface of the A-lamellae by the self epitaxial mechanism [6, 28]. Consequently, the B-lamellae grow on the base of the A-lamellae. Thus, the SAXS cross pattern appears during the stable  $\alpha$ -phase crystallization. Due to the higher supercooling, both lamellae have thinner spacing.

After the appearance of spontaneous  $\beta$ -nucleation, the orientated  $\beta$ -lamellae preferentially develop. In this case, A-lamellae are advantageous to grow because of the growth direction parallel to the z-axis, and thus the SAXS  $\beta$ -phase A-lamellae reflection is located on the equator.

## References

1. T. Seto, K. Asai and A. Mito, *Memoirs College of Science*, Univ. Kyoto, Ser. A, **28**, No. 1 (1956).
2. K. Tanaka, T. Seto and Y. Fujiwara, *Rep. Progress Polym. Phys. Jpn.*, **6**, 285 (1963).
3. K. Sasaguri, R. Yamada and R. S. Stein, *J. Appl. Phys.* **35**, 3188 (1964).
4. J. M. Crissman and E. Passaglia, *J. Res. Nat., Bur. Std.*, **70 A**, 225 (1966).
5. J. M. Crissman, *J. Polym. Sci., A-2*, **7**, 389 (1969).
6. Y. Fujiwara, *Kolloid-Zeit. Zeit. Polymer*, **226**, 135 (1968)
7. A. J. Lovinger, C. C. Gryte, *Macromolecules*, **9**, 247, (1976).
8. Y. Fujiwara, “*A Survey of Temperature Slope Crystallization for the Oriented Crystallization of Polymer Lamellae*”. Shizuoka University (1989)
9. Y. Fujiwara, *Polymer Bull.*, **13**, 253 (1985)
10. Y. Fujiwara, *Colloid & Polymer Sci.* **265**, 1027 (1987)
11. Y. Fujiwara, *Polymer Bull.*, **17**, 539 (1987)
12. Y. Fujiwara, *Colloid & Polymer Sci.*, **253**, 273 (1975)
13. Y. Fujiwara, T. Goto, and Y. Yamashita, *Polymer*, **28**, 1253 (1987)

14. T. Asano, T. Yamamoto, M. F. Mina, Y. Fujiwara, H. Takahashi and I. Hatta, *J. Macromol. Sci. PartB-Phys.*, **B38**, 163 (1999)
15. T. Asano, M.F. Mina, A. Nishida, S. Yoshida and Y. Fujiwara, *J. Macromol. Sci. PartB-Phys.*, **B40(3&4)**, 355 (2001)
16. T. Asano, *Polym. Bull.*, **10**, 547 (1983)
17. T. Asano and H. Abe, *J. Phys. Soc. Jpn.*, **53**, 1071 (1984)
18. T. Asano, *Polym. Bull.*, **12**, 543 (1984)
19. T. Asano, Y. Shibata, M.F. Mina, R. Nuryadi, *Rep. Fac. Sci., Shizuoka Univ.*, **33**, 33 (1999)
20. T. Asano, K. Imaizumi, N. Tohyama, S. Yoshida, *J. Macromol. Sci., PartB-Phys.* **B43(3)**, 639 (2004)
21. T. Asano, R. Nuryadi, M. F. Mina, *Rep. Fac. Sci., Shizuoka Univ.*, **32**, 45-51 (1998)
22. T. Yoshida, T. Asano, N. Miyashita, M. Matsu-ura, J. Kitabatake, I. Hatanaka, K. Seri, F. J. Baltá Calleja and L. Giri, *J. Macromol. Sci. PartB-Phys.*, **B36**, 789 (1997).
23. T. Asano, M. Kondo, M. Natsume, N. Tsumagari, M. M. Alam, C. Sawatari, A. Würflinger, *J. Macromol. Sci., PartB-Phys.* **B43(6)**, 1263 (2004)
24. K. G. Lee and J. M. Schultz, *Polymer*, **34**, 4455 (1993)
25. T. Hugel, G. Strobl, *Acta. Polym.*, **50**, 214, (1999)
26. H. D. Keith, *J. Appl. Phys.* **30**, 1485 (1959)
27. F. J. Padden and H. D. Keith, *J. Appl. Phys.*, **37**, 4013 (1966)
28. S. Yan, F. Katzenberg, J. Petermann, D. Yang, Y. Shen, C. Straupe, J. C. Wittmann, B. Lotz, *Polymer*, **41**, 2613, (2000).